Morphology and stability of droplets sliding on soft viscoelastic substrates

Mathieu Oléron, Laurent Limat, Julien Dervaux, Matthieu Roché

Soft Matter

ARTICLE TYPE

Cite this: DOI: 00.0000/xxxxxxxxxx

Morphology and stability of droplets sliding on soft viscoelastic substrates.

Mathieu Oléron, Laurent Limat, Julien Dervaux and Matthieu Roché‡

Received Date
Accepted Date

DOI: 00.0000/xxxxxxxxxx

We show that energy dissipation partition between a liquid and a solid controls the shape and stability of droplets sliding on viscoelastic gels. When both phases dissipate energy equally, droplet dynamics is similar to that on rigid solids. When the solid is the major contributor to dissipation, we observe an apparent contact angle hysteresis of viscoelastic origin. We find excellent agreement between our data and a non-linear model of the wetting of gels of our own that also indicates the presence of significant slip. Our work opens general questions on the dynamics of curved contact lines on compliant substrates.

An ever-increasing number of applications such as biofouling repellency[1,2], dew harvesting[3–5] and anti-icing[6] relies on the use of viscoelastic coatings. Not only do these materials confer controlled interfacial properties to their substrate, they may also be compliant enough to deform and dissipate energy after the deposition of a droplet[7–10], affecting both the equilibrium shape of the latter and the dynamics of the contact line between the solid, the liquid and the ambient fluid[11–13]. This coupling leads to unique substrate-droplet and droplet-droplet interactions[14–18].

The influence of substrate compliance on the shape and stability of moving droplets is hardly known. On a rigid plate inclined at an angle α with the horizontal, the morphology of sliding droplets is dictated by the dependence of the dynamic contact angle θ_d between the liquid-gas and solid-liquid interfaces on droplet velocity U and the ability of the trailing edge contact line to form corners, the radius of curvature of which was related to the nanometric scale at which the hydrodynamic description of wetting breaks down[19–25]. Beyond a threshold velocity, corners destabilize into rivulets that fragment into tinier droplets known as pearls[19,21,23,26–28]. These results hold for systems where energy dissipation occurs entirely in the liquid. However, on a gel with surface energy γ_s and shear modulus μ_0, deformations having a magnitude comparable to the elastocapillary length $\ell_s = \gamma_s/(2\mu_0)$ propagate with the contact line, leading to dissipation in the droplet and the substrate. Thus, we expect a more complex shape selection process.

Here we tune energy dissipation partition between the liquid and the solid and we show that this balance controls the morphology and stability of droplets sliding on soft solids. When both materials dissipate energy equally, droplet dynamics are akin to those reported on a rigid substrate, despite the compliance of the gel. When dissipation occurs only in the substrate, we observe an apparent contact angle hysteresis and the appearance of sharp features (corners, cusps...) only beyond the pearling instability threshold. We rationalize our results with a non-linear model of the wetting of soft solids of our own and find very good agreement. In all cases, our analysis points to the existence of significant slip in our systems due to the presence of free polymer chains in the gel. Finally we discuss the perspectives of our work regarding our understanding of wetting.

1 Materials and Methods

1.1 Properties of the liquids

We use pure glycerol (G100, Sigma Aldrich, G5516), a 60wt%-glycerol-in-water mixture (G60), polyethylene glycol-ran-propylene glycol (P25, PEG-ran-PPG, average molecular weight $M_w \sim 2500\,\mathrm{g\,mol^{-1}}$, Sigma Aldrich), a 70wt%-polyethylene glycol-ran-propylene glycol monobutyl ether-in-water mixture (P7, PEG-ran-PPG ME, Sigma Aldrich), and the UCON lubricant 75-H-90,000 (U90, Dow corning). Table 1 summarizes their properties. All the liquids are insoluble in silicone gels. These liquids are chosen to minimize the effects of evaporation and hygroscopy as much as possible. We measure the liquid-vapor surface tension γ with the pendant drop technique. We estimate the density ρ by weighing a volume $V = 10 \pm 0.5$ mL of liquid with a 0.01-g-accurate scale. We measure the dynamic viscosity η with a capillary viscosimeter sitting next to the set-up twice a day to account for hygroscopic and thermal effects.

1.2 Gel preparation

Gel slabs are prepared with a two-part commercial silicone kit (Dow Corning Sylgard 527). We mix equal volumes of each part of the kit together, as recommended by the manufacturer, in a

Matière et Systèmes Complexes, Université Paris Cité, CNRS UMR 7057, Paris, France

‡: to whom correspondence should be addressed: matthieu.roche@u-paris.fr

Table 1 Properties of liquids used in our experiments. Values for the equilibrium contact angle are extracted from the measurements of the dynamic contact angle as a function of velocity, see Materials and Methods for more details. The substrate in all cases is Sylgard 527 prepared following the manufacturer-recommended process. Its shear modulus is $\mu_0 = 1.077$ kPa, its relaxation time $\tau = 18.2$ ms, and the exponent characterizing its rheology $m = 0.626$.

	Surface tension γ mN m^{-1}	Viscosity η mPa s	Density ρ 10^3 kg m^{-3}	Equilibrium contact angle θ_{eq} °	Relaxation ratio $\mathcal{R}$
U90	40.7± 0.9	36900± 690	1.08± 0.05	61.6± 0.7	2.24± 0.42
P7	37.3± 0.2	842± 99	1.05± 0.05	56.6± 0.7	92.7± 11.0
G100	63.1± 0.5	631± 104	1.27± 0.06	97.2± 1.1	119± 20
P25	37.1± 0.4	491± 34	1.05± 0.01	64.3± 0.2	165± 11
G60	62.9± 0.1	6.8± 0.2	1.16± 0.06	98.1± 0.9	10700± 400

weighing boat previously cleaned with ethanol and water, and dried. The gel mixture is degassed under vacuum for 2 h to remove bubbles. It is then poured in a 60×40-mm^2 plastic vessel (Caubère), also cleaned with ethanol and distilled water and let to dry in a vacuum before use. Then, we leave the sample in an oven at 65 °C for 15 to 18 h. We perform experiments exclusively on dust-free unmarked gels.

1.3 Free-chain extraction

Soft silicone gels such as Sylgard 527 contain free mobile chains. The presence of mobile chains in silicone gels affects adhesion[29–31] and wetting. For example, a small amount of mobile chains can induce a transition between multiple sliding regimes[32,33]. Hence quantifying their amount is necessary. We extract free chains from silicone gels using the process described by Hourlier-Fargette *et al.*[32]. After weighing pieces of gels, we dip them into toluene (VWR, AnalaR NORMAPUR), a good solvent for PDMS. Free chains migrate to the solvent. We renew toluene everyday for five days to accelerate the extraction process. Then the sample is immersed in a mixture of toluene and ethanol (VWR, AnalaR NORMAPUR) to remove toluene from the gel. Ethanol is added progressively to avoid damaging the sample. We start with a solution of 20wt% ethanol in toluene, and we increase the ethanol proportion by steps of 20wt% every day, until the sample sits in 100% ethanol. After three baths in pure ethanol, the gel stops shrinking. We dry the gel under vacuum to remove the remaining solvent and weigh it again. From this procedure, we find that our materials contain 62wt% free chains. We note that these cleaned samples proved difficult to manipulate and did not allow us to perform systematic experiments, as the cleaning process would often lead to fracture, surface roughness, etc, in line with previous reports[34].

1.4 Rheology

We perform small amplitude oscillatory shear rheology on our gels with an Anton Paar MCR 501 rheometer mounted with a plate-plate geometry (diameter $d = 25$ mm). Strain amplitude is set at 1%. We extend the frequency range using a time-temperature superposition procedure[35]. We fit the data with the Chasset-Thirion model[36]:

$$G(\omega) = \mu_0(1 + (i\omega\tau)^m), \tag{1}$$

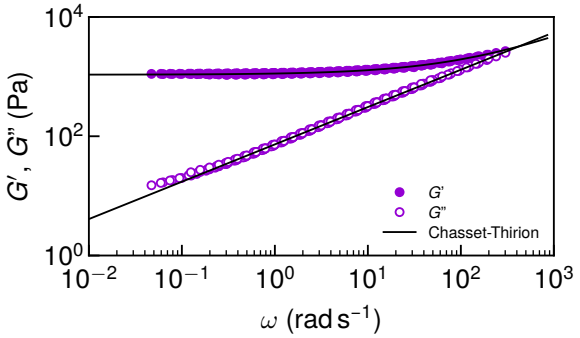

Fig. 1 Rheology of Sylgard 527. Storage modulus G' and loss modulus G" as function of pulsation ω. Strain amplitude: 1%. Continuous black lines: Chasset-Thirion law, Eqs. 2 and 3.

with G the complex modulus, ω the strain angular frequency and τ a characteristic relaxation time. The exponent m depends on the degree of polymerization of the polymer network and on the coordination number of monomers[36,37].

If we decompose the complex modulus $G(\omega)$ in a real elastic part $G'(\omega)$ and an imaginary dissipative part G"(ω), we obtain

$$G'(\omega) = \mu_0(1 + \cos(m\pi/2)(\omega\tau)^m), \tag{2}$$

$$G"(\omega) = \mu_0 \sin(m\pi/2)(\omega\tau)^m. \tag{3}$$

We determine τ and m by fitting the loss factor deduced from the model to its experimental value:

$$\frac{G"}{G'}(\omega) = \tan(\delta) = \frac{\sin(m\pi/2)(\omega\tau)^m \tan(m\pi/2)}{\sin(m\pi/2)(\omega\tau)^m + \tan(m\pi/2)}. \tag{4}$$

We inject the values of τ and m to fit equations 2 and 3 to the rheological data (Fig. 1). We find $\mu_0 = 1.077$ kPa, $\tau = 18.2$ ms, and $m = 0.626$.

1.5 Sliding experiments

We deposit a liquid droplet with a micropipette on the gel. The spherical radius R_0 of the droplets before deposition is of the order of the capillary length $\ell_c = (\gamma/(\rho g))^{1/2} \simeq 1.5$ mm of the liquids in all cases.The experiment starts when we tilt the gel at an angle α with the horizontal. A LED panel (Effilux) shines light on the sample from below, and a camera (Imaging Source, DMK 33UX174) records top views of the droplet with a spatial reso-

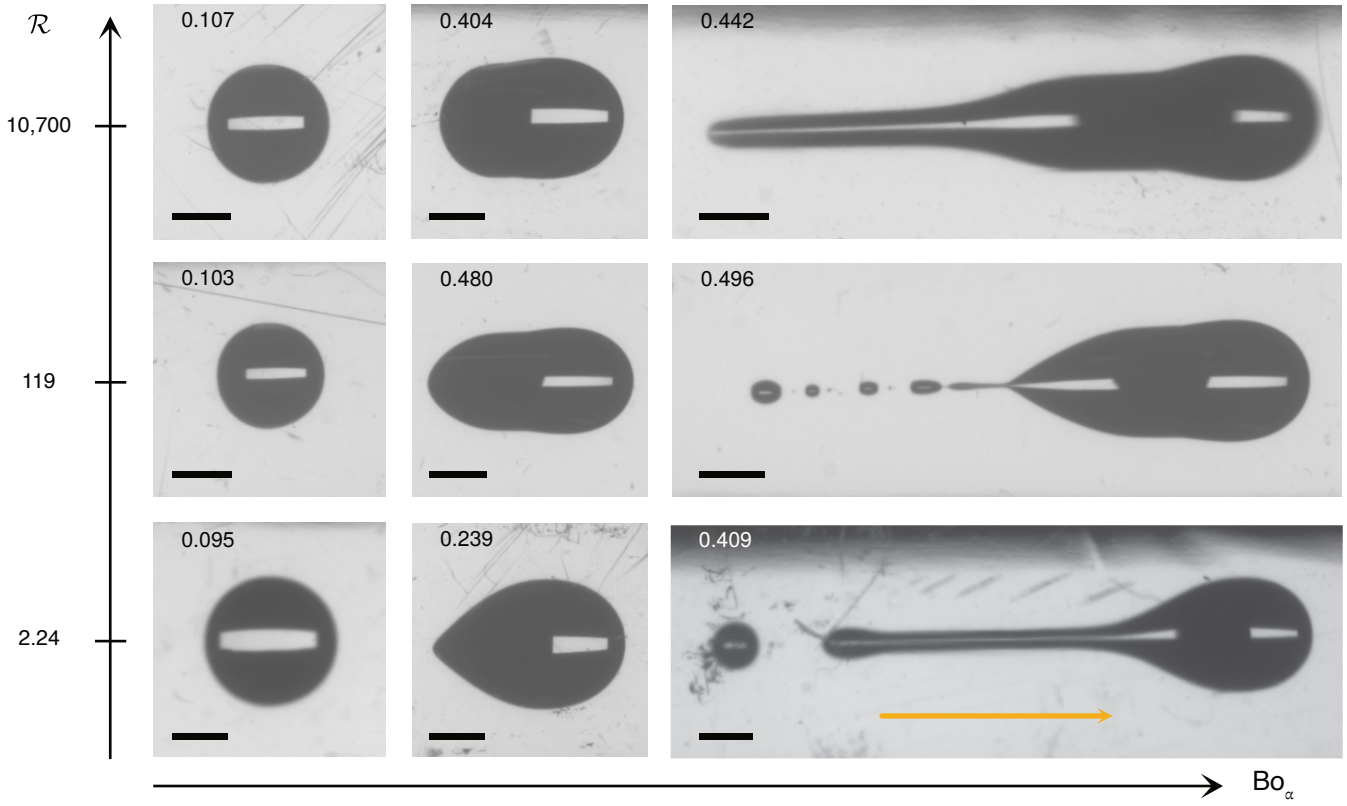

Fig. 2 Top view of droplets sliding on a silicone gel as a function of the Bond number Bo_α and the relaxation ratio $\mathcal{R}$. Each image displays the value of Bo_α. The pinch behind the front of the droplet at large $\mathcal{R}$ is an image artifact: the equilibrium contact angle is greater than $\pi/2$ for these systems and the liquid/air interface hangs over the moving contact line. Orange arrow: direction of motion. Scale bar: 2 mm.

lution of 32 μm px^{-1}. We take side views on some experiments (Imaging Source, DMK 33UX174, spatial resolution 4 μm px^{-1}). The thickness of all the samples, $h_s \sim 4$ mm, is much larger that the elastocapillary length of our material, $\ell_s \sim 10$ μm, to avoid small-thickness effects [16]. Samples are covered with a polystyrene lid that we find able to prevent surface ageing and dust deposition. We unmold gel layers and cut their edges so the meniscus is not in the way of side views. We obtain identical results when the silicone gel is in the box or unmolded.

We check the volume of droplets by weighing samples before droplet deposition and after. We track the motion of droplets with the software package FiJi [38]. Droplet velocities U range from 10^{-3} to 1 mm s^{-1}. In most cases, the trajectories that we observe are linear functions of time: droplets move at constant speed. For the longest experiments, drops may lose or gain water from surrounding air. In that case, we focus on early stages of the dynamics, when a steady state is reached . Thus we extract a single value U of the droplet velocity from each experiment. Each set of experimental conditions is tested three times to ensure reproducibility. The large amount of free chains present in our gels explains likely the absence of transition between two sliding regimes reported by Hourlier-Fargette *et al.* [32,33] in our experiments.

Sliding experiments are characterized by two dimensionless numbers, the Bond number

$$Bo_\alpha = \frac{\rho g R_0^3}{\gamma R_c} \sin\alpha, \tag{5}$$

and the liquid capillary number

$$Ca = \frac{\eta U}{\gamma}, \tag{6}$$

that compare capillary stresses to gravitational and viscous ones respectively. Here, g is the acceleration of gravity, R_0 is the radius of the spherical droplet before deposition, and R_c is the contact radius between the droplet and the substrate. Energy dissipation partition between the two media is characterized by the relaxation ratio $\mathcal{R}$ [39] that compares the viscocapillary relaxation velocity in the liquid, $U_l = \gamma/\eta$, to that in the solid, $U_s = \ell_s/\tau$, giving

$$\mathcal{R} = \frac{\gamma\tau}{\eta\ell_s}. \tag{7}$$

Contact line motion has been studied in the limit $\mathcal{R} \to \infty$ in the literature [40,41], *i.e.* energy dissipation in the liquid is neglected. The liquids we use allow us to vary $\mathcal{R}$ over four orders of magnitude (Table 1).

1.6 Equilibrium contact angle measurements

Dynamic contact angles are measured at the front and trailing edges of the droplet, on the side-view images. Wetting equilibrium is difficult to identify on these systems using classical techniques such as droplet deposition. We see the contact line moving even a few hours after deposition. We circumvent this issue by measuring the dynamic contact angles as close as possible to

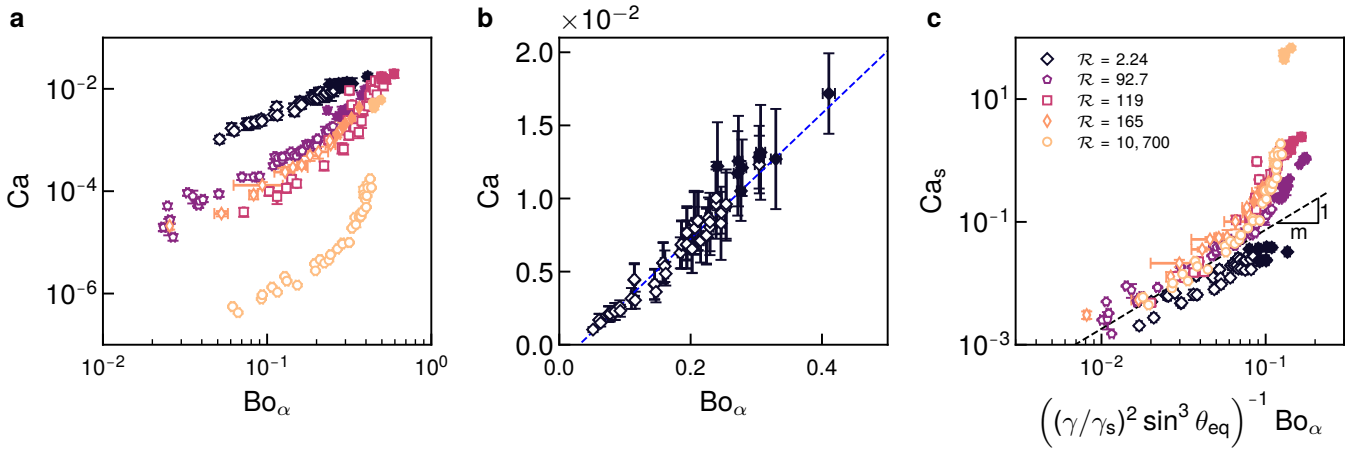

Fig. 3 (a) Dependence of the liquid capillary number Ca on the Bond number Bo_α. (b) Focus on the case $\mathcal{R} \simeq 2$. Blue dashed line: Eq. 9. (c) Dependence of the solid capillary number Ca_s on the Bond number Bo_α. Dashed line: Eq. 13. In all panels, filled symbols correspond to points measured above the pearling threshold. (a) and (c) share the same legend.

$U = 0$. Then we fit the points around $U = 0$ with a linear law, and estimate the value of the contact angle at $U = 0$. With this method, we still do not have access to the true equilibrium contact angle. Indeed, while we never observe droplet pinning, contact hysteresis may still be present, hence inducing uncertainty on the real equilibrium value of the contact angle, θ_{eq}, and allowing us to estimate only the range over which the static contact angle θ_s varies. However, our measurements constrain the range over which θ_s varies. We find this range to be of the order of 3 to 5 $^\circ$ for all of our systems. Given this narrow range, we assume that $\theta_{eq} = \theta_s$ in the rest of the paper.

2 Results

Droplet shapes carry obvious signatures of changes in the magnitude of $\mathcal{R}$ (Fig. 2). While droplets remain nearly axisymmetric at small Bond numbers, symmetry is lost as Bo_α increases. When $\mathcal{R} \simeq 2$, a corner appears at the trailing edge. In contrast, the aft and fore radii of curvature of the droplets are comparable when $10^2 \leq \mathcal{R} \leq 10^4$. Besides, the droplet contour contains portions parallel to the direction of motion, leading to shapes similar to those observed in the case of droplets sliding on hysteretic surfaces [26,42–44]. A further increase of Bo_α at all values of $\mathcal{R}$ leads to the observation of the pearling instability.

Figure 3a shows that, for equivalent Bond numbers, liquid capillary numbers vary over four orders of magnitude as the relaxation ratio changes by the same amount. The data for $\mathcal{R} \simeq 2$ suggest an affine relation between Ca and Bo_α (Fig.3b), similar to the rigid case [19,23] where the non-zero y-intercept is a signature of contact hysteresis, and hence droplet pinning. However, we never observe the latter in our experiments, suggesting that this non-zero intercept is either the signature of a contact angle hysteresis with an amplitude smaller than our resolution or the manifestation of another contribution in the force balance. The functional form for the other datasets is more complex. We multiply $\mathcal{R}$ with Ca to obtain a capillary number for the solid, $Ca_s = U\tau/\ell_s$ and plot the data in Figs. 3a-b as a function of this quantity. Accounting for variations of the equilibrium contact angle θ_{eq} from one system to another, we observe a collapse of the large-$\mathcal{R}$ data on a single master curve (Fig. 3c). We can discriminate the curve obtained for $\mathcal{R} \simeq 2$, in line with the assumption that the power balance between viscous dissipation in the liquid and gravity, relevant to these experiments, differs from the balance between viscous dissipation in the solid and gravity tested in the $Ca_s(Bo_\alpha)$ representation.

Another way to characterize the dynamics of sliding droplets is to measure the dependence of the dynamic contact angle on droplet velocity. Figure 4a shows the deviation from the equilibrium contact angle θ_{eq} as a function of the capillary number Ca, for each system. We observe that the apparent dynamic contact angle θ_d increases smoothly as the capillary number goes from negative to positive values when $\mathcal{R} \simeq 2$. Corners appear when $Ca \geq 7.5 \times 10^{-3}$, a value of the same order of magnitude as those reported for fluoropolymer-coated silicon wafers [19,21,23]. The other curves display a steep jump of several tens of degrees around $Ca = 0$ that brings to mind results obtained in the case of significant wetting hysteresis [45] and when a contact line moves on low-modulus natural rubber and *cis*-butadiene [46]. In a vein similar to what we observed in figure 3, the datasets collapse on a master curve when plotted against the solid capillary number Ca_s (Fig. 4b). The curve obtained at $\mathcal{R} \sim 10^4$ displays plateaus in the advancing and receding branches, similar to those reported in earlier studies [12].

3 Discussion

3.1 $\mathcal{R} \simeq 2$: a deceptive resemblance to the rigid case.

The data presented in figure 3 can be discussed in terms of scaling laws. We focus first on the case $\mathcal{R} \simeq 2$, and we follow a rationale proposed in studies of droplets sliding on rigid substrates [19,23] in which we assume that dissipation occurs entirely in the liquid and balances the gravitational force experienced by the droplet. Contact-angle hysteresis may also be present. The force balance

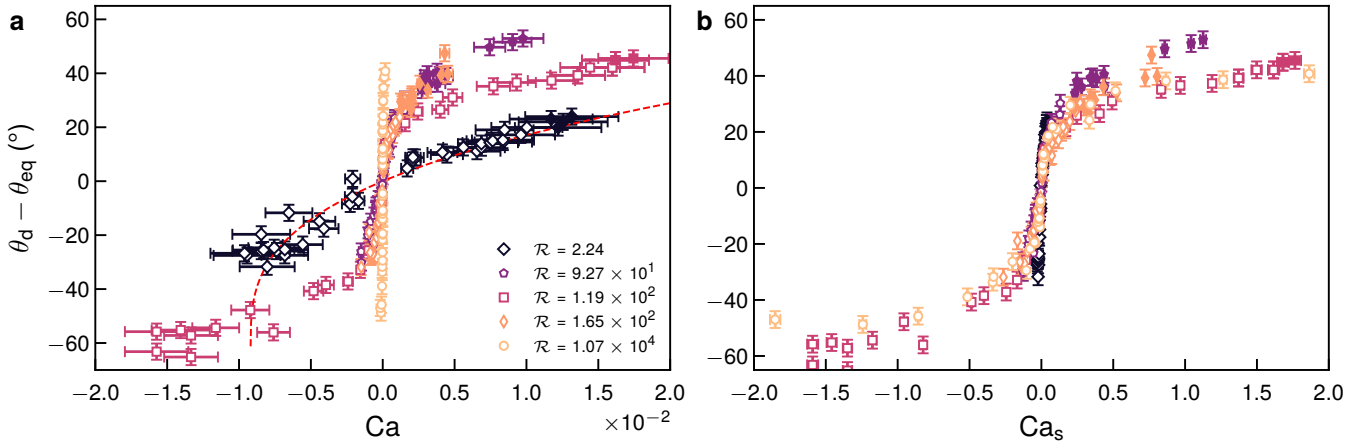

Fig. 4 (a) Dependence of the deviation from the equilibrium contact angle $\theta_d - \theta_{eq}$ on the liquid capillary number Ca. Positive (resp. negative) Ca values correspond to advancing (resp. receding) contact lines. Filled symbols: points measured above the pearling threshold. Red dashed line : fit of the Cox-Voinov law (Eq. 10) to the $\mathcal{R} \simeq 2$ data. (b) Same data as in a plotted against the solid capillary number Ca_s. Both figures share the same legend.

then reads:

$$\rho g R_0^3 \sin\alpha \sim \eta \frac{U}{h} R_c^2 + \gamma(\cos\theta_a - \cos\theta_r) R_c. \tag{8}$$

with U/h the velocity gradient between the liquid/gas interface and the substrate, and θ_a and θ_r the advancing and receding dynamic contact angles, *i.e.* the threshold values of the contact angle above and below which contact line motion occurs.

After rearrangements and non-dimensionalization, this force balance leads to (see Appendix)

$$Ca \sim \frac{1-\cos\theta_{eq}}{\sin\theta_{eq}} [Bo\alpha - Bo_c] \tag{9}$$

where Bo_c is a threshold Bond number for droplet motion below which the droplet is pinned by contact angle hysteresis [42].

Scaling 9 captures well the trend of the data obtained for $\mathcal{R} \simeq 2$ (Fig. 3b). We can estimate the magnitude of the contact angle hysteresis of silicone gels from Bo_c [23,47] (See Eq. 24 in Appendix) and we find $\Delta\theta = \theta_a - \theta_r \simeq 3.5$ °, a value compatible with the constraint on hysteresis amplitude imposed by the data displayed in Fig. 5. Indeed, we noted earlier that we never observe droplet pinning. This absence still allows us to provide an upper bound on the range of real contact angle hysteresis. The estimate of $\Delta\theta$ is also consistent with the shapes of droplets at $\mathcal{R} \simeq 2$, which display no signature of hysteresis [44] (Fig. 2), and reports in the literature regarding silicone gels [1,16].

Given the similarities between the $\mathcal{R} \simeq 2$ data and the rigid case, we push the comparison further by testing the contact angle dependence on the capillary number to the Cox-Voinov law [23,48,49]:

$$\theta_d^3 - \theta_{eq}^3 = 9 Ca \ln\left(\frac{h}{\lambda}\right), \tag{10}$$

where h is the height on the liquid/vapor interface at which the angle is measured and λ is a nanoscopic length scale introduced to circumvent stress divergence at the contact line. The agreement is qualitatively excellent. However, the logarithmic term has an amplitude around 15. As we measure the contact angle at $h \sim 100$ µm, we obtain an unreasonable cutoff length scale $\lambda \simeq 30$ pm, smaller than an interatomic bond. The large value of the logarithmic term likely results from the fact that $\mathcal{R} \sim 1$: dissipation in the solid is of the same order of magnitude as in the liquid. Failure of the Cox-Voinov law is then expected, as it does not account for all dissipation sources. Note that we can go back to the $Ca(Bo\alpha)$ data in Fig. 3b and fit them with a more refined version of Eq. 9 (Eq. 21 in Kim *et al.* [20]),

$$Ca \sim \frac{2}{3c(\theta)\ln\frac{L}{\lambda}} [Bo\alpha - Bo_c], \tag{11}$$

where L is the horizontal extent of the wedge near the contact line in which the stress balance involves only capillary and viscous stresses, *i.e.* a distance of the order of the capillary length [50]. $c(\theta)$ is a monotonic decreasing function of the contact angle θ that characterizes the dependence of dissipation on the shape of the region near the contact line, assumed to be a wedge with an opening angle equal to θ. Following Kim *et al.* [20], we assume that $\theta \sim \theta_{eq}$. Then, $c(\theta) \simeq 0.6$ for the system we consider here. We also obtain an unreasonable value of the logarithmic term, up to some unidentified prefactors. Hence, while the data obtained at low values of $\mathcal{R}$ resemble those obtained with a rigid substrate, detailed analysis demonstrates that the agreement is only qualitative and that some physics realted to dissipation in the substrate is missing.

3.2 $\mathcal{R} >> 1$: the substrate contributes the most to dissipation.

In the limit $\mathcal{R} \to \infty$, energy dissipates in the substrate. A reasoning similar to the one used in the previous paragraph leads to a force balance that involves viscous dissipation in the solid and droplet weight [16]:

$$\rho g R_0^3 \sin\alpha \sim \mu_0 R_c \ell \left(\frac{\gamma}{\gamma_s}\sin\theta_{eq}\right)^3 \left(\frac{U\tau}{\ell_s}\right)^m. \tag{12}$$

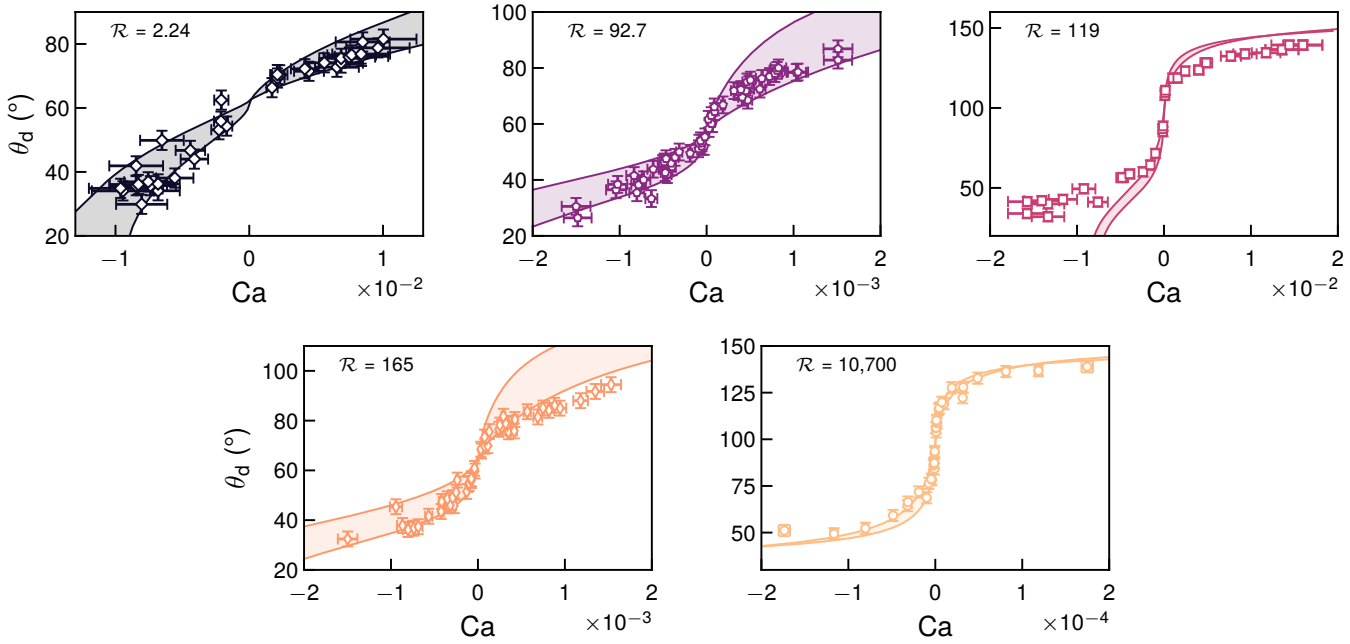

Fig. 5 Comparison between experimental dynamic contact angles θ_d and Eq. 14. The fitting parameter is the microscopic cutoff length scale, $\lambda = 100$ nm for all systems. Colored areas: fit spread reflecting experimental uncertainties.

After rearrangements and non-dimensionalization, we obtain the following scaling (See Appendix):

$$Bo_\alpha \sim \left(\frac{\gamma}{\gamma_s}\right)^2 (\sin\theta_{eq})^3 {Ca_s}^m, \tag{13}$$

where m is the exponent of the power law describing the loss modulus of the substrate as a function of strain frequency. For systems where $\mathcal{R} \geq 10^2$, Eq. 13 captures our data up to $Bo_\alpha \simeq 8 \times 10^{-2}$ (Fig. 3c).

3.3 Comparison with a non-linear model of wetting.

We compare the data in Fig. 5 to a model that we proposed recently[39] that describes the wetting of soft solids in a regime of finite strains under the assumption that γ_s is independent of strain: there is no Shuttleworth effect[51]. This analytic model relies on an asymptotic expansion of the quantities describing the mechanics of the substrate in terms of a power series of the ratio of the surface tension of the liquid to that of the solid, γ/γ_s. The model can also deal with arbitrary equilibrium contact angles. We assume that shear stresses in the bulk of the substrate become singular at the tip of the ridge because of an abrupt change of the sign of the slope of the substrate surface. This singularity leads to the existence of a finite viscoelastic force, $\mathcal{F}_{ve}$, exerted by the bulk of the substrate on the moving contact line, on top of the capillary force, $\mathcal{F}_{cap}$, that works to restore the equilibrium shape of the ridge that has rotated due to dissipation. The model provides an analytic prediction for the dependence of θ_d on $\mathcal{R}$ and Ca:

$$g(\theta_d) = g\left(\frac{\pi}{2} + f(\mathcal{F}_{cap}(\mathcal{R}Ca,\Lambda),\mathcal{F}_{ve}(\mathcal{R}Ca,\Lambda),\theta_{eq})\right) + Ca\ln\left(\frac{h}{\lambda}\right), \tag{14}$$

with $g(x) = \int_0^x \frac{z-\sin(z)\cos(z)}{2\cos(z)}dz$ and Λ the ratio between the thickness of the substrate h_s to the elastocapillary length ℓ_s. The reader should refer to the appendix for more extensive information on functions $f(\mathcal{F}_{cap},\mathcal{F}_{ve},\theta_{eq})$ and $g(\theta_d)$. Equation 14 is formally similar to the general form of the Cox-Voinov relation, where the first r.h.s. term is related to the microscopic contact angle and the second results from dissipation in the liquid[52]. Here, the microscopic angle term is a dynamic quantity set by the response of the solid to the propagation of the ridge. The correction to this term increases as $\mathcal{R}$ increases. In our experiments, the thickness of the substrate is much greater than the elastocapillary length, $\Lambda \to \infty$. Then both $\mathcal{F}_{cap}$ and $\mathcal{F}_{ve}$ scale as $(\mathcal{R}Ca)^m = {Ca_s}^m$ in the limit $\mathcal{R}Ca << 1$ while they both converge to the same constant value $m/(2(1-m))$ when $\mathcal{R}Ca \to \infty$. The series expansion of $g(\theta_d)$ when $\mathcal{R}Ca \to 0$ shows that we expect a regime dominated by dissipation in the solid around $\mathcal{R}Ca = 0$ for all non-zero values of $\mathcal{R}$, with $g(\theta_d) \propto (\mathcal{R}Ca)^m$. As the velocity increases, we expect to observe either a regime similar to that of a liquid spreading on a rigid substrate and described by the Cox-Voinov relation, Eq. 10, in the limit $\mathcal{R} \to 0$, or a regime that saturates to a constant value dependent on the exponent m of the rheology in the advancing branch, $\mathcal{R}Ca > 0$ and falls down quickly to 0 in the receding branch when $\mathcal{R} \to \infty$.

Figure 5 shows that the agreement between the experimental data and Eq. 14, setting $\lambda = 100$ nm, is good to excellent for all

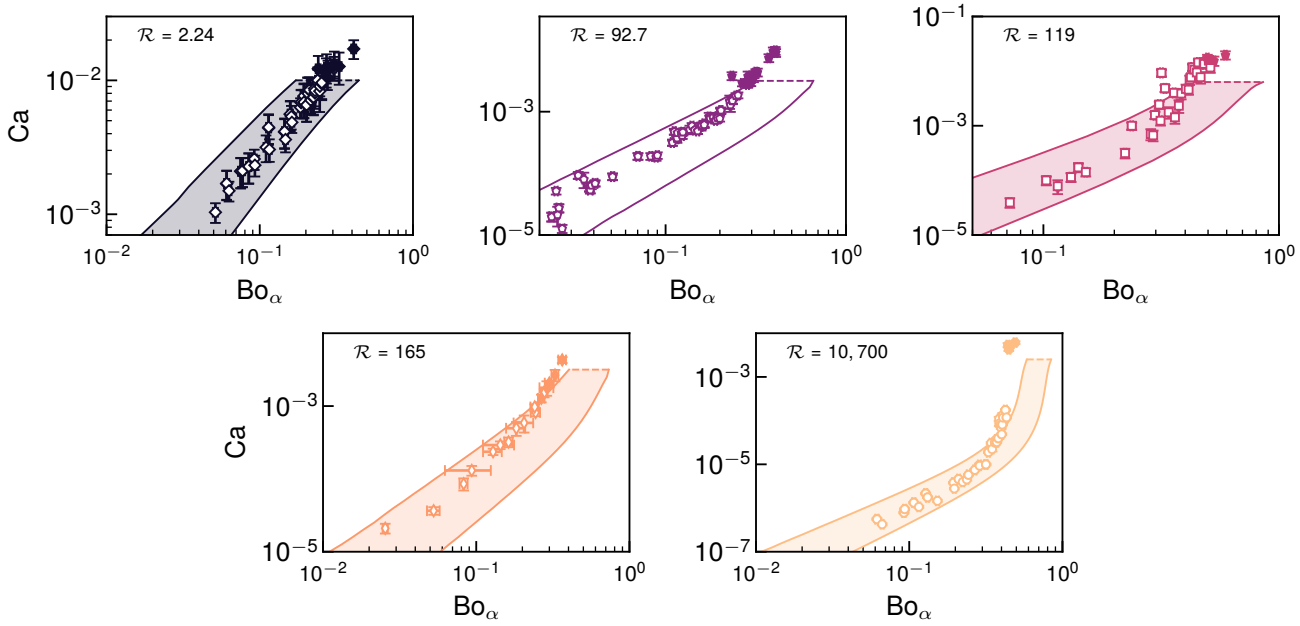

Fig. 6 Comparison between the data of Fig. 3 with the non-linear model of Dervaux *et al.*[39]. Closed symbols represent data points obtained beyond the pearling threshold. The fitting domains represent the variation of the fitting results due to uncertainty on the experimental parameters. Dashed lines: pearling threshold capillary number.

datasets. The steepness of the $\mathcal{R} >> 1$ curves close to $Ca = 0$ is characteristic of what we called "soft hysteresis" in a previous paper[39], *i.e.* the steepening of the $\theta_d(Ca)$ curves around $Ca = 0$ because of dissipation in the solid. We emphasize that this is no true hysteresis. Rather, figure 5 for $\mathcal{R} = 10,700$ shows that an abrupt and continuous variation of the dynamic contact angle in the region around $Ca_s = 0$ connects two flatter portions of the curve; these flatter parts are connected by a discontinuous jump in the case of real hysteresis. Nonetheless, the signature of this abrupt contact angle variation on droplet shape is akin to that of real hysteresis (Fig. 2). These results and their interpretation shine new light on the nature of the hysteresis reported for soft materials in the past literature. The study of Extrand and Kumagai[46] characterizes the inclination of a soft substrate beyond which a droplet starts to slide. In their set-up, substrate inclination changes over time at a fixed rate, and their experiments last from 10 to 30 s. In our case, experiments at the smallest inclinations last several hours and we can still observe droplet motion. Droplet pinning is absent in our experiments. Our results highlight the necessity of reaching and measuring the smallest possible velocities to characterize wetting dynamics on soft solids accurately. We note that the model fails to capture the receding branch $Ca < 0$ for $\mathcal{R} = 119$. The trailing edge of these droplets oscillates close to the pearling transition, and our model does not predict this response.

The fitting procedure also suggests that all systems, even at small values of $\mathcal{R}$, exhibit a steep asymptote at $Ca = 0$. This is because viscoelastic dissipation in the solid, $\propto U^m$ with $m < 1$, always exceeds viscous dissipation in the liquid, $\propto U$, at vanishing Ca. We note that the value of $\Delta\theta$ obtained from Eq. 9 is compatible with the jump magnitude seen in the fit of the model to the data for $\mathcal{R} \simeq 2$, despite the issues that we have identified. This comparison indicates that signatures of soft hysteresis on droplet dynamics are akin to those of real, defect-induced, hysteresis. Figure 6 shows that the model can also predict the full range of the data displayed in Fig. 3.

Finally, fits to the datasets with Eq. 14 are obtained while keeping λ constant. We can also set experimental parameters to their nominal value and leave λ free to adjust. We find best-fit values $50 \leq \lambda \leq 1000$ nm, larger than the molecular sizes of the liquids we use, of the order of 10 nm at most, and smaller than the elastocapillary length $\ell_s \simeq 20$ µm. The large magnitude of λ is likely the result of the presence of free chains that lubricate the gel-droplet contact and induce slip[2,32,53,54], in a manner similar to liquid-infused surfaces[55].

3.4 Properties of the system at the pearling threshold.

Characterization of the properties of the system at the pearling threshold shows how different the transition to liquid deposition on soft substrates is from that on rigid ones. First, the contact angle just before pearling, θ_c, is around 32° when the relaxation ratio $\mathcal{R} \leq 10^2$ and rises up to 50° when $\mathcal{R} \simeq 10^4$ (Fig. 7a). These values are much larger than those, around 10°, reported for rigid substrates[23]. Second, the threshold capillary number $|Ca_c|$ depends on both the equilibrium contact angle θ_{eq} and $\mathcal{R}$ (Fig. 7b). While the former is expected[56] and may at least partly explain the jump of around an order of magnitude in $|Ca_c|$ at $\mathcal{R} \sim 100$, the latter remains to be investigated. For $\mathcal{R} \simeq 2$, $|Ca_c| \simeq 1.1 \times 10^{-2}$, around twice as large as in the rigid case for a comparable equilibrium contact angle θ_{eq}[23]. Keeping the latter constant, a one-hundredfold increase of $\mathcal{R}$ decreases $|Ca_c|$ tenfold. This trend is in agreement with our model. Indeed, the latter predicts that, for a constant equilibrium contact angle, the capillary number at which a zero receding contact angle is attained decreases as R increases. Besides, predictions for the contact angle curves are

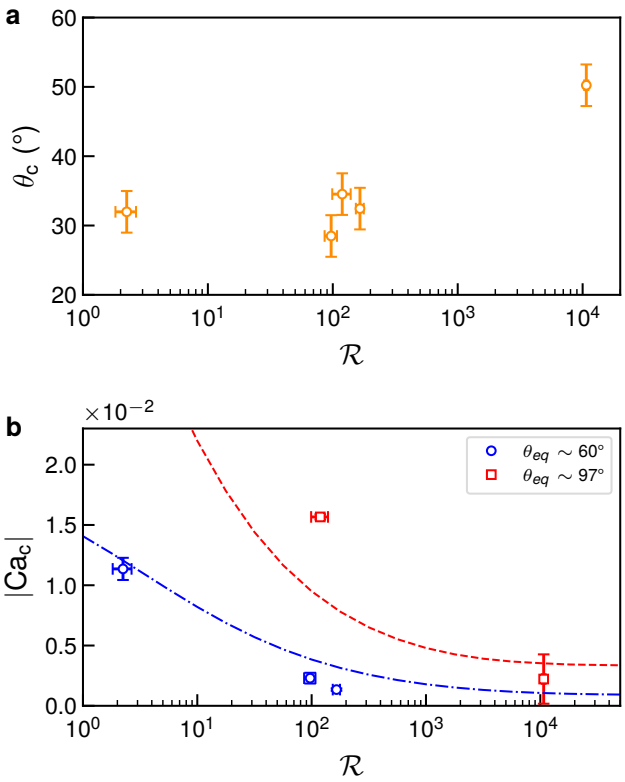

Fig. 7 (a) Receding contact angle θ_c and (b) capillary number Ca_c at the pearling threshold as a function of the relaxation ratio $\mathcal{R}$. θ_c: receding contact angle of the last stable point; Ca_c: mean of the capillary numbers of the last stable and the first unstable points. Error on the latter: standard deviation. Dashed lines: prediction based on Eq. 14 of the vanishing-contact-angle capillary number.

steep in the vicinity of this capillary number. Sensible changes in the contact lead to small changes in Ca. This rationale explains why the prediction of our model for the zero-contact-angle receding capillary number captures quite well the data (Fig. 7b): while the last value of the receding contact before destabilization differs from 0, the capillary number is expected to be similar. Finally, dissipation in the substrate increases the sensitivity of droplets to the pearling instability.

4 Conclusion and Outlook

In conclusion, we document how droplets slide on soft viscoelastic gels as a function of energy dissipation partition between the liquid and the substrate. While the substrate is always deformable, sliding droplets display shapes and dynamics akin to those observed on a rigid solid when dissipation occurs equally in both materials. When the substrate is the main dissipative element, straight lines parallel to the direction of motion appear in the droplet contour as the signature of an apparent hysteresis in the dependence of dynamic contact angles on velocity. The ability of a non-linear model that we proposed recently to describe the data very well suggests that accounting for geometrical nonlinearities is enough to describe droplet dynamics on soft substrates, without the need to assume a dependence of the surface energy of the solid on strain, in line with recent experimental results[57]. The model accounts at least qualitatively for the lubricating effect of free chains present in our system. This issue is currently attracting a lot of interest[32,53,54]. Droplet motion seems possible only in the presence of mobile chains that act as a liquid infusing the surface. The way the thickness of the liquid layer is set and its relation to slip in soft gels is still a rather open question[54].

Our study raises questions around the physics of curved contact lines. On rigid substrates, the trailing edge contact angle decreases almost to zero at the pearling transition threshold. We show that the path to fragmentation is different on a soft gel. Our observations suggest that the curvature of the trailing edge is constrained by the substrate, an issue that calls for future work. The tenfold increase of the capillary number when passing the pearling threshold at $\mathcal{R} \simeq 10^4$ also deserves investigation, as we were not able to find a smooth transition.

Author Contributions

J. D., L. L. and M. R. acquired the funding supporting this research; M.O., J.D., L.L. and M.R. conceptualized research; M.O. carried out the experiments; J. D., L. L. and M. R. supervised the work; M.O., J.D., L.L. and M.R. analyzed the data; M. O. wrote the initial draft of the paper; M.O., J.D., L.L. and M.R. reviewed and edited the paper.

Conflicts of interest

There are no conflicts to declare.

Acknowledgements

We thank L. Bergougnoux and E. Guazzelli for providing UCON U90. We are grateful to H. Montès for performing the time-temperature rheology of Sylgard 527. ANR (Agence Nationale de la Recherche) and CGI (Commissariat à lInvestissement dAvenir) are gratefully acknowledged for their financial support through the GelWet grant (ANR-17CE30-0016).

Appendix

Scaling laws for the $Ca(Bo\alpha)$ curves in the limit $\mathcal{R} \to 0$.

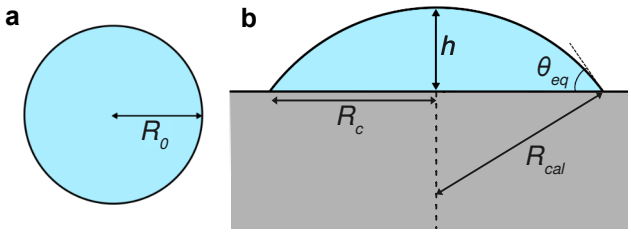

Fig. 8 Different configurations for a liquid drop. (a) A spherical droplet of volume $V = 4R_0^3/3\pi$. (b) The same droplet as a spherical cap after spreading on a substrate, with radius of curvature $R_{\rm cal}$, height at the center h, contact radius R_c and contact angle θ_{eq}.

In experiments, a droplet of volume V is deposited on the substrate. This volume corresponds to a sphere of radius R_0 (Fig. 8a). Once it has spread on the surface of the substrate, the droplet reaches its equilibrium shape, a spherical cap with radius $R_{\rm cal}$, height h, contact radius R_c and contact angle θ_{eq} (Fig. 8b).

R_c is difficult to measure in experiments, especially when the equlibrium contact angle is larger than $\pi/2$. In contrast, we can obtain R_0 by weighing the drop. If we know the equilibrium contact angle θ_{eq}, we can write, assuming that droplets form spherical caps after deposition:

$$\begin{cases} R_c = R_{\text{cal}} \cos\left(\frac{\pi}{2} - \theta_{eq}\right) \\ R_{\text{cal}} - h = R_{\text{cal}} \sin\left(\frac{\pi}{2} - \theta_{eq}\right). \end{cases} \tag{15}$$

Rearranging, we can link the contact radius and the height of the droplet to the spherical cap radius:

$$\begin{cases} R_c = R_{\text{cal}} \sin\theta_{eq} \\ h = R_{\text{cal}}(1-\cos\theta_{eq}). \end{cases} \tag{16}$$

Now, we can express the volume for both a sphere and a spherical cap:

$$\begin{cases} V = \frac{4\pi}{3} R_0^3 \\ V = \frac{\pi}{3} h^2 (3R_{\text{cal}} - h) \end{cases} \tag{17}$$

in terms of R_c and θ_{eq}:

$$\begin{cases} V = \frac{4\pi}{3} R_0^3 \\ V = \frac{\pi R_c^3}{3} \frac{(2+\cos\theta_{eq})(1-\cos\theta_{eq})^2}{\sin^3\theta_{eq}}. \end{cases} \tag{18}$$

Volume conservation then leads to:

$$\frac{R_c}{R_0} = \frac{1}{f(\theta_{eq})} = \sin\theta_{eq} \left(\frac{(2+\cos\theta_{eq})(1-\cos\theta_{eq})^2}{4} \right)^{-\frac{1}{3}}. \tag{19}$$

Injecting Eq. 19 into the definition of the Bond number, Eq. 5, we obtain an expression for the Bond number that accounts for changes in the equilibrium contact angle:

$$Bo_\alpha = f(\theta_{eq}) \frac{\rho g R_0^2}{\gamma} \sin\alpha. \tag{20}$$

Now, let's assume that the gravitational force experienced by the droplet is balanced by dissipation in the liquid and contact angle hysteresis:

$$\rho g R_0^3 \sin\alpha \sim \eta \frac{U}{h} R_c^2 + \gamma(\cos\theta_a - \cos\theta_r) R_c. \tag{21}$$

Here U/h estimates the velocity gradient in the droplet, and θ_a and θ_r are the advancing and receding dynamic contact angles, *i.e.* the threshold values of the contact angle above and below which contact line motion occurs.

In what follows, we assume that the values of dynamic contact angles are close to that of the equilibrium contact angle, a hypothesis that is valid at low droplet velocities, $Ca << 1$. Thus, we can use the description of the equilibrium shape of the droplet to relate the contact angle and the contact radius. Using Eq. 16, we obtain:

$$\frac{R_c}{h} = \frac{\sin\theta_{eq}}{1-\cos\theta_{eq}}. \tag{22}$$

Dividing both sides of Eq. 21 by the liquid-vapor surface tension γ, replacing R_c/h, and using Eq. 19, we find that

$$Ca \sim \frac{1-\cos\theta_{eq}}{\sin\theta_{eq}} [Bo_\alpha - Bo_c], \tag{23}$$

where Bo_c is a threshold Bond number below which contact hysteresis pins the droplet to the surface. A similar scaling was first suggested in Podgorski *et al.* [19]. We observe that this correction leads to the overlap of our data for $\mathcal{R} \simeq 2$ and theirs (Fig. 9). Following Dussan V. [47] and Le Grand *et al.* [23], we can evaluate contact angle hysteresis from the experimental value of Bo_c using:

$$Bo_c = \left(\frac{24}{\pi}\right)^{1/3} \frac{(\cos\theta_r - \cos\theta_a)(1+\cos\theta_a)^{1/2}}{(2+\cos\theta_a)^{1/3}(1-\cos\theta_a)^{1/6}}. \tag{24}$$

Le Grand *et al.* [23] performed this estimation accounting for the prefactor appearing in front of Bo_α when fitting their data with Eq. 23. We use the same procedure to obtain our estimate.

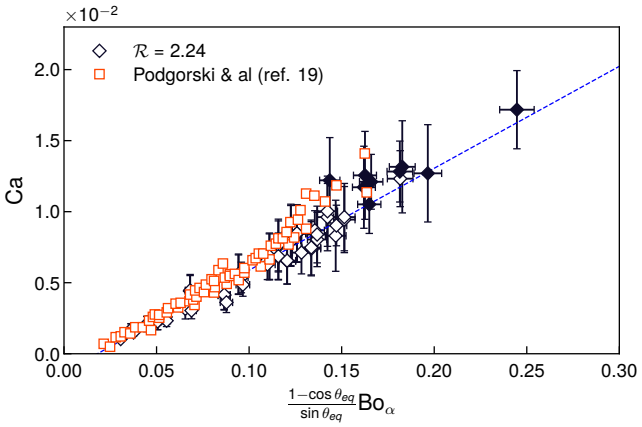

Fig. 9 Comparison between our data for $\mathcal{R} \simeq 2$ and the data of Podgorski *et al.* [19] once corrections related to a different equilibrium contact angle are accounted for. The blue dashed line is a guide for the eye.

Scaling laws for the $Ca(Bo_\alpha)$ curves in the limit $\mathcal{R} \to \infty$.

We expect that the relation between injected energy and dissipation be modified when the effective viscosity of the solid exceeds that of the liquid. The collapse of the $Ca - Bo_\alpha$ curves in the $Ca_s - Bo_\alpha$ space, with $Ca_s = \mathcal{R}Ca$, suggests that the latter is a good metric. Besides, we know from the previous section that the equilibrium contact angle matters. Hence we should derive a scaling law for the solid-dominated case that accounts for all of these modifications. Note that we use again the approximation that the dynamic contact angles remain close to the equilibrium contact angle.

Inspired by Ref. [16], we estimate the power dissipated per unit of volume of the solid when the drop moves by a length ℓ:

$$d\mathcal{P}_{\text{diss}} \sim \sigma \varepsilon^2 \omega \tag{25}$$

with σ the viscous stress, ε the strain and ω the pulsation. Using

the Chasset-Thirion model:

$$G(\omega) = \mu_0(1 + (i\omega\tau)^m), \tag{26}$$

and taking the typical strain scale to be:

$$\varepsilon \sim \frac{\gamma}{\gamma_s}\sin\theta_{eq} \tag{27}$$

and the characteristic pulsation of the experiment as:

$$\omega = \frac{U}{\ell_s}, \tag{28}$$

we have the following estimate for viscous stresses in the solid:

$$\sigma \sim \mu_0 \left(\frac{U\tau}{\ell_s}\right)^m. \tag{29}$$

Then we have:

$$d\mathcal{P}_{\text{diss}} \sim \mu_0 \left(\frac{U\tau}{\ell_s}\right)^m \left(\frac{\gamma}{\gamma_s}\sin\theta_{eq}\right)^2 \frac{U}{\ell_s}. \tag{30}$$

Dissipation takes place in a half-torus having a radius R_c, width ℓ and height ℓ_r. As elasticity balances the vertical component of the resulting capillary force per unit length at the contact line $\gamma\sin(\theta_{eq})$, the height of the ridge scales as:

$$\ell_r \sim \gamma\sin\theta_{eq}/\mu_0. \tag{31}$$

Then, we can estimate the power dissipated in the solid, neglecting numerical prefactors:

$$\mathcal{P}_{\text{diss}} \sim \sigma\varepsilon^2\omega R_c\ell_r\ell \tag{32}$$

$$\mathcal{P}_{\text{diss}} \sim \mu_0 U R_c\ell \left(\frac{\gamma}{\gamma_s}\sin\theta_{eq}\right)^3 \left(\frac{U\tau}{\ell_s}\right)^m. \tag{33}$$

Now, we can write the force balance that a droplet sliding on a viscoelastic substrate should obey. Dividing $\mathcal{P}_{\text{diss}}$ by the sliding velocity U, we have:

$$\rho g R_0^3 \sin\alpha \sim \mu_0 R_c\ell \left(\frac{\gamma}{\gamma_s}\sin\theta_{eq}\right)^3 \left(\frac{U\tau}{\ell_s}\right)^m. \tag{34}$$

Dividing by the liquid-vapor surface tension γ and the contact radius R_c on both sides and rearranging, we obtain:

$$Bo_\alpha \sim \frac{\mu_0\ell}{\gamma} \left(\frac{\gamma}{\gamma_s}\sin\theta_{eq}\right)^3 \left(\frac{U\tau}{\ell_s}\right)^m \tag{35}$$

and using:

$$\frac{U\tau}{\ell_s} = \mathcal{R}Ca = Ca_s, \tag{36}$$

we end up with the following prediction:

$$Bo_\alpha \sim \frac{\mu_0\ell}{\gamma} \left(\frac{\gamma}{\gamma_s}\sin\theta_{eq}\right)^3 {Ca_s}^m. \tag{37}$$

The prefactor $[(\gamma/\gamma_s)\sin(\theta_{eq})]^3$ in Eq. 37 should capture the dependence on equilibrium contact angles. In the limit of thick samples, $\ell = \ell_s = \frac{\gamma_s}{2\mu_0}$ [16], and we obtain Eq. 13 in the main text when neglecting numerical prefactors:

$$Bo_\alpha \sim \left(\frac{\gamma}{\gamma_s}\right)^2 (\sin\theta_{eq})^3 {Ca_s}^m. \tag{38}$$

Full expression of function $f(\mathcal{F}_{cap}, \mathcal{F}_{ve})$

Below, we provide the full expression of the function f that appears in Eq. 14:

$$f(\mathcal{F}_{cap}, \mathcal{F}_{ve}, \theta_{eq}) =$$

$$\arctan\left(\frac{-1+\sqrt{1+4\mathcal{A}^2-4\mathcal{A}\cos\theta_{eq}}}{\sqrt{2(-1+2\mathcal{A}\cos\theta_{eq}+\sqrt{1+4\mathcal{A}^2-4\mathcal{A}\cos\theta_{eq}})}}\right) \tag{39}$$

where the dependence on the two forces $\mathcal{F}_{cap}$ and $\mathcal{F}_{ve}$ lies in the function

$$\mathcal{A} = \frac{\gamma}{\gamma_s}(\mathcal{F}_{cap}(\mathcal{R}Ca, \Lambda) + \mathcal{F}_{ve}(\mathcal{R}Ca, \Lambda)) \tag{40}$$

The expressions of $\mathcal{F}_{cap}$ and $\mathcal{F}_{ve}$ can be found in Dervaux *et al.* [39], Eqs. 45 and 46. The form 39 of function f reduces to the form found in Eq. 64 in Dervaux *et al.* [39] when $\theta_{eq} = \pi/2$.

We note that the argument of function g is written $(\pi/2 + \ldots)$ not because the equilibrium contact angle is equal to $\pi/2$ but rather because we use the following trigonometric identity to write its final form:

$$\arctan x + \arctan\frac{1}{x} = \frac{\pi}{2} \tag{41}$$

Notes and references

1 N. MacCallum, C. Howell, P. Kim, D. Sun, R. Friedlander, J. Ranisau, O. Ahanotu, J. J. Lin, A. Vena, B. Hatton, T.-S. Wong and J. Aizenberg, *ACS Biomater. Sci. Eng.*, 2015, **1**, 43–51.

2 N. Lavielle, D. Asker and B. D. Hutton, *Soft Matter*, 2021, **17**, 936–946.

3 M. Sokuler, G. K. Auernhammer, M. Roth, C. Liu, E. Bonacurrso and H.-J. Butt, *Langmuir*, 2010, **26**, 1544–1547.

4 A. Phadnis and K. Rykaczewski, *Langmuir*, 2017, **33**, 12095–12101.

5 C. S. Sharma, A. Milionis, A. Naga, C. W. E. Lam, G. Rodriguez, M. F. Del Ponte, V. Negri, H. Raoul, M. D'Acunzi, H.-J. Butt, D. Vollmer and D. Poulikakos, *Adv. Funct. Mater.*, 2022, **32**, 2109633.

6 *Ice Adhesion: Mechanism, Measurement and Mitigation*, ed. K. Mittal and C.-H. Choi, Wiley, 1st edn., 2020.

7 A. Carré, J. C. Gastel and M. E. R. Shanahan, *Nature*, 1996, **379**, 432–434.

8 D. Long, A. Ajdari and L. Leibler, *Langmuir*, 1996, **12**, 1675–1680.

9 R. W. Style, R. Boltyanskiy, Y. Che, J. S. Wettlaufer, L. A. Wilen and E. R. Dufresne, *Phys. Rev. Lett.*, 2013, **110**, 066103.

10 S. J. Park, B. M. Weon, J. S. Lee, J. Lee, J. Kim and J. H. Je, *Nat. Commun.*, 2014, **5**, 5369.

11 A. Carré and M. E. R. Shanahan, *Langmuir*, 2001, **17**, 2982–2985.

12 S. Karpitschka, S. Das, M. van Gorcum, H. Perrin, B. Andreotti and J. H. Snoeijer, *Nat. Commun.*, 2015, **6**, 7891.

13 J. Dervaux and L. Limat, *Proc. R. Soc. A*, 2015, **471**, 20140813.

14 R. W. Style, Y. Che, S. J. Park, B. M. Weon, J. H. Je, C. Hyland, G. K. German, M. P. Power, L. A. Wilen, J. S. Wettlaufer and E. R. Dufresne, *Proc. Natl. Acad. Sci.*, 2013, **110**, 12541–12544.

15 S. Karpitschka, A. Pandey, L. A. Lubbers, J. H. Weijs, L. Botto, S. Das, B. Andreotti and J. H. Snoeijer, *Proc. Natl. Acad. Sci.*, 2016, **113**, 7403–7407.

16 M. Zhao, J. Dervaux, T. Narita, F. Lequeux, L. Limat and M. Roché, *Proc. Nat. Acad. Sci. U.S.A.*, 2018, **115**, 1748–1753.

17 K. Smith-Mannschott, Q. Xu, S. Heyden, N. Bain, J. H. Snoeijer, E. R. Dufresne and R. W. Style, *Phys. Rev. Lett.*, 2021, **126**, 158004.

18 H. K. Khattak, S. Karpitschka, J. H. Snoeijer and K. Dalnoki-Veress, *Nat. Commun.*, 2022, **13**, 4436.

19 T. Podgorski, J.-M. Flesselles and L. Limat, *Phys. Rev. Lett.*, 2001, **87**, 036102.

20 H.-Y. Kim, H. J. Lee and B. H. Kang, *Journal of Colloid and Interface Science*, 2002, **247**, 372–380.

21 E. Rio, A. Daerr, B. Andreotti and L. Limat, *Phys. Rev. Lett.*, 2005, **94**, 024503.

22 J. H. Snoeijer, E. Rio, N. Le Grand and L. Limat, *Phys. Fluids*, 2005, **17**, 072101.

23 N. Le Grand, A. Daerr and L. Limat, *J. Fluid Mech.*, 2005, **541**, 293–315.

24 I. Peters, J. Snoeijer, A. Daerr and L. Limat, *Phys. Rev. Lett.*, 2009, **103**, 114501.

25 K. Winkels, I. Peters, F. Evangelista, M. Riepen, A. Daerr, L. Limat and J. Snoeijer, *Eur. Phys. J. Spec. Top.*, 2011, **192**, 195–205.

26 B. A. Puthenveettil, V. K. Senthilkumar and E. J. Hopfinger, *J. Fluid Mech.*, 2013, **726**, 26–61.

27 H. Kim, C. Poelma, G. Ooms and J. Westerweel, *J. Fluid Mech.*, 2015, **762**, 393–416.

28 W. Liang and S. Tietze, *Sci Rep*, 2017, **7**, 14164.

29 A. Galliano, S. Bistac and J. Schultz, *J. Adhes.*, 2003, **79**, 973–991.

30 Q. Zhang and L. A. Archer, *Langmuir*, 2007, **23**, 7562–7570.

31 K. E. Jensen, R. Sarfati, R. W. Style, R. Boltyanskiy, A. Chakrabarti, M. K. Chaudhury and E. R. Dufresne, *Proc. Natl. Acad. Sci.*, 2015, **112**, 14490–14494.

32 A. Hourlier-Fargette, A. Antkowiak, A. Chateauminois and S. Neukirch, *Soft Matter*, 2017, **13**, 3484–3491.

33 A. Hourlier-Fargette, J. Dervaux, A. Antkowiak and S. Neukirch, *Langmuir*, 2018, **34**, 12244–12250.

34 A. Tiwari, L. Dorogin, A. I. Bennett, K. D. Schulze, W. G. Sawyer, M. Tahir, G. Heinrich and B. N. J. Persson, *Soft Matter*, 2017, **13**, 3602–3621.

35 M. Rubinstein and R. H. Colby, *Polymer Physics*, Oxford University Press Inc., New York, USA, 2003.

36 J. G. Curro and P. Pincus, *Macromolecules*, 1983, **16**, 559–562.

37 J. G. Curro, D. S. Pearson and E. Helfand, *Macromolecules*, 1985, **18**, 1157–1162.

38 J. Schindelin, I. Arganda-Carreras, E. Frise, V. Kaynig, M. Longair, T. Pietzsch, S. Preibisch, C. Rueden, S. Saalfeld, B. Schmid, J. Y. Tinevez, D. J. White, V. Hartenstein, K. Eliceiri, P. Tomancak and A. Cardona, *Nat. Methods*, 2012, **9**, 676–682.

39 J. Dervaux, M. Roché and L. Limat, *Soft Matter*, 2020, **16**, 5157–5176.

40 R. W. Style, A. Jagota, C. Y. Hui and E. R. Dufresne, *Annu. Rev. Condens. Matter Phys.*, 2017, **8**, 99–118.

41 B. Andreotti and J. H. Snoeijer, *Annu. Rev. Fluid Mech.*, 2020, **52**, 285–308.

42 E. B. Dussan V. and R. T.-P. Chow, *J. Fluid Mech.*, 1983, **137**, 1–29.

43 T. Podgorski, *Ph.D. thesis*, Université Paris 6, 2000.

44 G. Ahmed, M. Sellier, M. Jermy and M. Taylor, *Euro J Mech B Fluid*, 2014, **48**, 218–230.

45 H. B. Eral, D. J. C. M. 't Mannetje and J. M. Oh, *Colloid Polym Sci*, 2013, **291**, 247–260.

46 C. W. Extrand and Y. Kumagai, *Journal of Colloid and Interface Science*, 1996, **184**, 191–200.

47 E. B. Dussan V., *J. Fluid Mech.*, 1985, **151**, 1–20.

48 O. V. Voinov, *Fluid Dyn.*, 1976, **11**, 714–721.

49 R. G. Cox, *J. Fluid Mech.*, 1986, **168**, 169–194.

50 A. Pelosse, É. Guazzelli and M. Roché, *J. Fluid Mech.*, 2023, **955**, A7.

51 R. Shuttleworth, *Proc. Roy. Soc. A*, 1950, **63**, 444–457.

52 D. Bonn, J. Eggers, J. Indekeu, J. Meunier and E. Rolley, *Rev. Mod. Phys.*, 2009, **81**, 739–805.

53 Z. Cai and J. T. Pham, *ACS Appl. Polym. Mater.*, 2022, **4**, 3013–3022.

54 L. Hauer, Z. Cai, A. Skabeev, D. Vollmer and J. T. Pham, *Phys. Rev. Lett.*, 2023, **130**, 058205.

55 S. Hardt and G. McHale, *Annu. Rev. Fluid Mech.*, 2022, **54**, 83–104.

56 J. H. Snoeijer, N. Le Grand-Piteira, L. Limat, H. A. Stone and J. Eggers, *Phys. Fluids*, 2007, **19**, 042104.

57 N. Bain, A. Jagota, K. Smith-Mannschott, S. Heyden, R. W. Style and E. R. Dufresne, *Phys. Rev. Lett.*, 2021, **127**, 208001.